PAPER • OPEN ACCESS

Droplet-based assembly of magnetic superballs

To cite this article: S Schyck *et al* 2024 *J. Phys. Mater.* **7** 015003

View the article online for updates and enhancements.

You may also like

Journal of Physics: Materials

Droplet-based assembly of magnetic superballs

S Schyck[1] , J-M Meijer[2] , M P M Schelling[2] , A V Petukhov[3] and L Rossi[1,*]

[1] Department of Chemical Engineering, Delft University of Technology, Delft, The Netherlands
[2] Department of Applied Physics and Science Education and Institute for Complex Molecular Systems, Eindhoven University of Technology, Eindhoven, The Netherlands
[3] Debye Institute for Nanomaterials Science, Utrecht University, Utrecht, The Netherlands
[*] Author to whom any correspondence should be addressed.

E-mail: l.rossi@tudelft.nl

Abstract

The self-assembly of materials driven by the inherent directionality of the constituent particles is of both practical and fundamental interest because it enables the fabrication of complex and hierarchical structures with tailored functionalities. By employing evaporation assisted self-assembly, we form opal-like structures with micro-sized magnetic superball particles. We study the structure formation of different superball shapes during evaporation of a dispersion droplet with *in-situ* small angle x-ray scattering with microradian resolution in the absence and presence of an external magnetic field. In the absence of a magnetic field, strong shape-dependent structures form as the water evaporates from the system. Applying a magnetic field to the droplet has a unique effect on the system; strong magnetic fields inhibit the growth of well-ordered assemblies due to the formation of out-of-equilibrium dipolar structures while lower magnetic fields allow particles to rearrange and orient without inhibition. In this work, we show how the superball assembly inside a droplet can be controlled by the magnetic field strength and the superball shape. The tunability of these parameters not only enables the controllable formation of macroscopic colloidal assemblies but also opens up possibilities for the development of functional materials with tailored properties on a macro-scale.

1. Introduction

Designing the structure of colloidal assemblies is a crucial step towards controlled development of novel micro-structured materials and devices. In general, spherical particles assemble into a compact structure through either a face-centered cubic (fcc) or hexagonal close-packed arrangement, providing a way to engineer photonic crystals capable of specific functions [1, 2]. As a result, 3D assemblies of isotropic, spherical particles have demonstrated fascinating optical properties, acting as optical waveguides [3] and functioning as long-pass optical filters [4]. We can further explore a rich world of structural diversity by adding anisotropy to the constituent particles, such as a non-spherical shape or an intrinsic directionality via an internal magnetic moment [2, 5, 6]. One such anisotropic shape experimentally accessible on the colloidal scale is the superball which is a family of shapes that encompasses the transition from a sphere to a cube via a rounded cube [7]. Superballs have been shown to form a plastic crystal (or rotator) phase prior to their densest packing [8], which is a rhombohedral-like packing that progresses continuously from an fcc lattice (as spheres) to a simple cubic (SC) lattice (as perfect cubes) [7, 9–12]. Superballs possessing additional directional anisotropy, such as an internal magnetic moment, can lead to different dense packing. For micron-sized magnetic superballs, Meijer *et al* [13] showed the presence of hexagonally stacked layers that transform into long-range ordered body-centered monoclinic (BCM) lattices in the presence of an applied magnetic field for 3D assemblies induced by sedimentation in capillaries. In addition, for paramagnetic nanocubes, Ahniyaz *et al* [14] showed that an applied magnetic field induced the formation of highly ordered SC superlattices when assembled by a controlled solvent evaporation method.

The resultant macro- and micro-structure can be further influenced by the employed assembly technique [15]. Specifically, particle confinement within an evaporating droplet is one promising method for creating free-standing colloidal assemblies which can find applications as photonic devices, drug delivery, and magneto-optical materials [16–18]. These droplet-based assemblies are created using either substrate-free processes, such as ultrasonic levitation and emulsification [19–21], or substrate-based methods like deposition on a superhydrophobic surface [22, 23]. For the latter, the final shape of the assemblies can be varied by modifying the size of the droplet pinning site or the initial particle concentration, resulting in spheres, donuts, and mushrooms [1, 24, 25]. The internal structure of assemblies inside evaporating droplets is dependent on the droplet size and the dispersed particles' properties. For example, spherical particles have been shown to organize into their typical bulk dense packing or form novel icosahedral clusters depending on particle concentration [21, 26, 27]. For anisotropic truncated nanocubes, both bulk evaporation and droplet confinement assembly techniques lead to well-ordered fcc lattices [28].

We predict that the combination of anisotropic colloids and confinement induces the formation of more complex self-assembled structures. In our previous work [29], we observed that micron-sized silica superballs, inside evaporating droplets, assembled into close-packed structures, with the packing becoming increasingly more SC-like depending on the superball shape. However, these structures also exhibit a high degree of poly-crystallinity. Here, we increase the complexity of the system by assembling micron-sized superball particles with a magnetic dipole moment in spherical confinement. We utilized *in-situ* synchrotron small-angle x-ray scattering with micro-radian resolution (μrad-SAXS) to investigate the crystallization process. For dispersions of varying superball shapes, we collected scattering profiles over the droplet height as it evaporates in the absence and presence of an applied magnetic field. Our results show that the combination of confinement and magnetic interactions provides unique control over the final superstructures which is of interest for the fabrication of designer materials as well as photonic structures.

2. Methods

2.1. Particle synthesis
Hematite superball particles were prepared following the sol-gel procedure [30–32]. Silica shells were grown on hematite superball following to obtain m-values between 2.8 and 3.7 [33–35]. The complete particle synthesis procedure can be found in reference [35]. The obtained particles were characterized by transmission electron microscopy (Philips TECNAI12/20) and particle properties as described in supplementary table S1.

2.2. Sample preparation
Superball particles were dispersed in Milli-Q water at 0.005 vol% and 15 vol%. Capillary samples for form factor measurements were prepared by dispersing a 0.05 vol% particle dispersion inside a flame sealed glass capillary (0.20×4.00 mm, CM Scientific).

2.3. Droplet-based assembly
Superhydrophobic substrates with contact angles above 160° were prepared as described in reference [29]. Aqueous droplets of 1.5 μL with 15 vol% concentration of superball particles were deposited on superhydrophobic surfaces for drying. A custom-made set-up [13] consisting of permanent magnets was used to apply a horizontally oriented magnetic field ranging between $14 - 35$ mT during the drying process. The droplets were positioned at the center of the setup, where the magnetic field is uniform and constant throughout the droplet.

2.4. Small angle x-ray scattering measurements
SAXS measurements using a microradian setup [36] employing compound refractive lenses [37] were conducted at the beamline BM-26B DUBBLE [38] at the European Synchrotron Radiation Facility in Grenoble, France. During these experiments, the incident x-ray beam with a photon energy of 13.96 keV ($\lambda = 0.886$ Å) was focused on a Photonic Science CCD detector with 4008×2671 pixels and a pixel size of 9×9 μm at a distance of 7.87 m. The detector was protected from the direct beam by a wedge-shaped beam-stop. Substrates with the drying droplets were placed horizontally in the x-ray beam. Measurements were performed in the droplets during the full evaporation process over the height of the droplet with z-steps of 0.1 mm. Background measurements for droplet assemblies were taken with plain water droplets at various heights and for capillary experiments with plain water filled capillaries. Form factors of superballs were collected from dilute particle dispersions (0.005 vol%) in glass capillaries immediately after preparation.
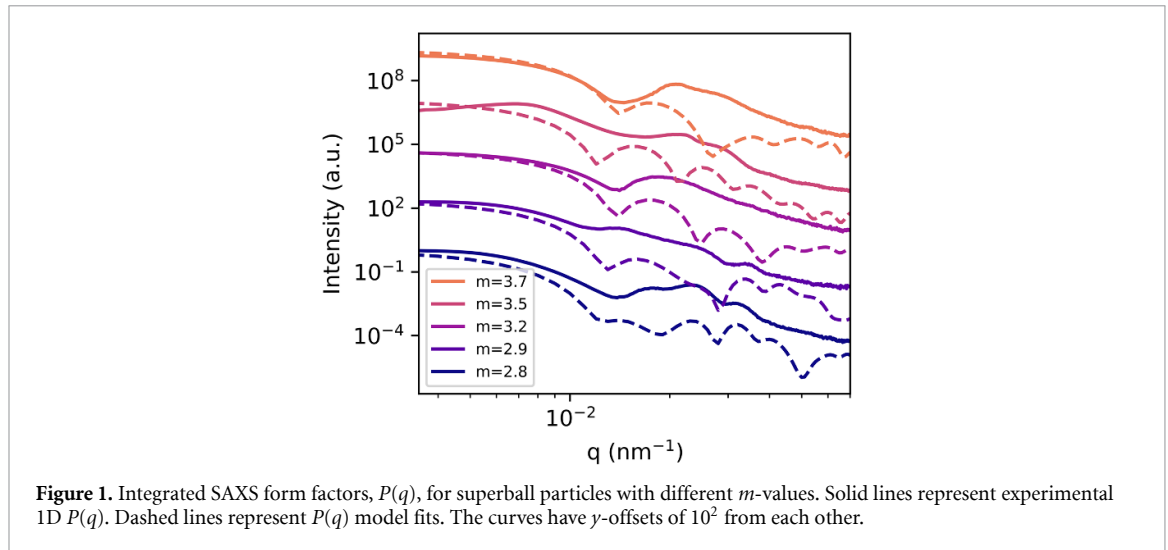
Figure 1. Integrated SAXS form factors, $P(q)$, for superball particles with different m-values. Solid lines represent experimental 1D $P(q)$. Dashed lines represent $P(q)$ model fits. The curves have y-offsets of 10^2 from each other.
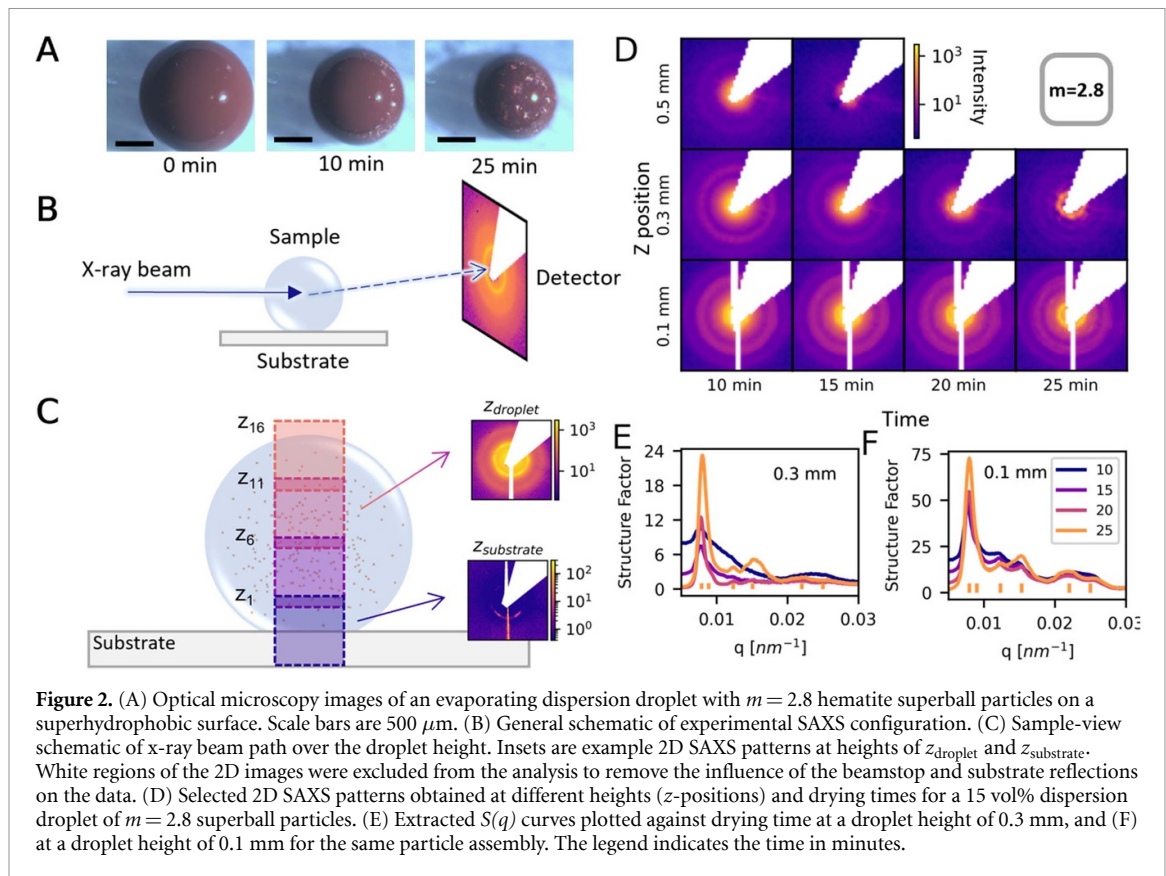
3. Results and discussion

3.1. Superball properties

To study the self-assembly process of magnetic superballs, we synthesized five different hematite-silica core–shell superball particles. The shape of a superball particle is defined by $\left(\frac{x}{a}\right)^m + \left(\frac{y}{a}\right)^m + \left(\frac{z}{a}\right)^m \geqslant 1$ where a is $1/2$ the distance between opposite faces, and m is the shape parameter [7, 39]. For hematite superballs, the magnetic dipole was found to be positioned at a 12° angle into the cube face from one of the internal diagonals of the cube [32]. In order to prevent superball aggregation due to strong magnetic dipole-dipole attractions and generate a range of m-values, we coated the magnetic hematite superball seeds with a silica layer of various thickness. As we increase the silica shell thickness, t, we decrease the m-value of the superball particles (supplementary figure S1). To characterize the superball particles' assembly, we use SAXS with microradian resolution. In general for SAXS measurements, the scattering intensity, $I(q)$, obtained from a collection of discrete particles is dependent on the form factor, $P(q)$, and the structure factor, $S(q)$. $P(q)$ is determined by the particles' shape and size, and $S(q)$ is determined by the structure that the particles form. Here, we approximate $I(q) \propto \phi_{\text{particle}} \cdot P(q) \cdot S(q)$ where ϕ_{particle} is the particle volume fraction [19]. To determine the structure of assembled superballs, we decouple $S(q)$ from $I(q)$ by obtaining $P(q)$ curves from dilute suspensions (<0.01 wt%) of particles where $S(q) = 1$. Figure 1 displays the collected $P(q)$ curves for all investigated particles. For core–shell particles, $P(q)$ depends on the silica shell thickness (t), inner shape (m_{inner}), and outer shape (m_{outer}) [8, 40].

The hematite cores in particles with $m = 2.8$, 2.9, and 3.2 are identical, and the final particle size and shape are mainly determined by the thickness of the silica shell layer. To understand the influence of the silica shell and hematite core on the form factor, we calculated their form factor numerically using a model based on a volume integration of a cloud of scatters [8, 10, 41, 42] (supplementary figure S1). With this method, we modeled the isotropic form factor, $P(q)$, similar to our experimental core–shell superballs denoted by the dashed lines in figure 1. Here, we observed that the size and shape of the hematite core particle strongly affect the overall shape of the $P(q)$, and the silica shell introduces additional oscillations in the $P(q)$ depending on t. We also noted that the deviations observed between the model and the experimental data could be attributed to slight variations in the particle polydispersity, both in terms of the shape and size of the superballs, as well as in the model's population of random scatterers present in the shell compared to the core. When the thickest shell layer is used ($m = 2.8$ and $t = 187$ nm, dark blue curve), we observe several oscillations after the initial valley, which is due to a stronger contribution of the silica shell to the form factor. On the other hand, for the same hematite core particle with a thinner shell ($m = 3.2$), we observe more uniform $P(q)$ peaks initially due to a larger contribution from the hematite core particle. These small differences between particles results in large variations of the $P(q)$ and highlight the importance of collecting sample specific form factors for complex anisotropic systems.
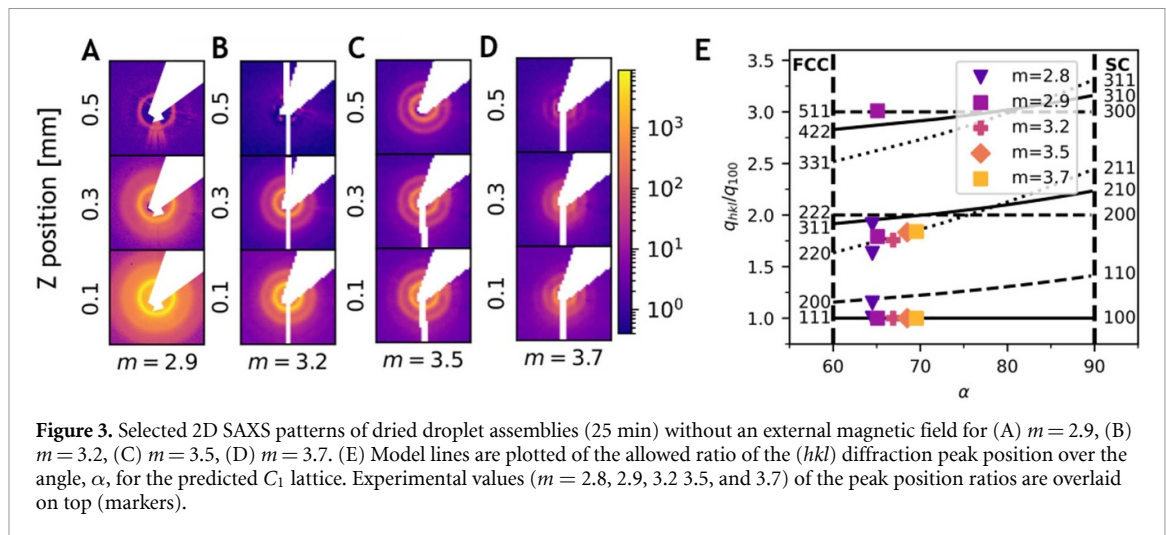
3.2. Effect of droplet confinement

To investigate the structure formation and drying process of assembling superballs in dispersion droplets, we conducted *in-situ* SAXS measurements, tracking the scattering patterns at different heights within the droplet. As water evaporates from the droplet, figure 2(A) shows the drying dispersion droplet that forms a

Figure 2. (A) Optical microscopy images of an evaporating dispersion droplet with $m = 2.8$ hematite superball particles on a superhydrophobic surface. Scale bars are 500 μm. (B) General schematic of experimental SAXS configuration. (C) Sample-view schematic of x-ray beam path over the droplet height. Insets are example 2D SAXS patterns at heights of $z_{droplet}$ and $z_{substrate}$. White regions of the 2D images were excluded from the analysis to remove the influence of the beamstop and substrate reflections on the data. (D) Selected 2D SAXS patterns obtained at different heights (z-positions) and drying times for a 15 vol% dispersion droplet of $m = 2.8$ superball particles. (E) Extracted $S(q)$ curves plotted against drying time at a droplet height of 0.3 mm, and (F) at a droplet height of 0.1 mm for the same particle assembly. The legend indicates the time in minutes.

spherical macro-structure of assembled superballs. We note that assemblies formed by this technique may result in a variety of shapes, e.g. spheres, donuts, and mushrooms, based on the contact pinning size and the particle concentration [22, 23]. Throughout this work, our aim was to maintain a nearly spherical shape during drying. We also found that some assemblies experienced slight cavitation, as discussed in the supplementary information and figure S2. Additionally, we observe iridescent colors on the surface of the droplet as it dries which persists after complete drying (figure 2(A)). This coloration is a result of Bragg scattering of light, serving as a clear indication of ordered structure formation [4, 22]. We note that hematite particles possess a higher density than water, which might imply a dominant role for sedimentation in assembly. However, prior studies indicate that assembly behavior is influenced by a combination of factors, including the elasticity of the shell of particles formed at the droplet interface, an introversion process influenced by pressure gradients, and the suppression of evaporation rates [43–45].

SAXS measurements (figure 2(B)) were collected over the height of the droplet using a 0.5 mm beam size with a 0.1 mm step size as shown in figure 2(C). We observed scattering at different heights originating from two distinct sources: the assembly of particles inside the dispersion droplet, occurring at heights designated as $z_{droplet}$, and the scattering predominantly generated by the superhydrophobic substrate, occurring at heights denoted as $z_{substrate}$. To analyze the drying process of the droplet, we tracked the change in droplet height by measuring the maximum height of $z_{droplet}$ at a z-step 0.1 mm before the beam left the droplet, based on the intensity of the scattering pattern. In reality, scattering from the substrate already appears around four steps above the substrate due to the beam size being larger than the step size, visible by significant vertical flares and low intensity values in the 2D SAXS pattern. For simplicity, we have denoted $z = 0$ to correspond to the height immediately above the substrate ($z_{substrate}$) where scattering from the droplet is still visible and scattering from the substrate is minimal.

The typical evolution of the 2D SAXS patterns as a function of z-height and time for a drying dispersion droplet containing magnetic superball particles with $m = 2.8$ is shown in figure 2(D). At $z = 0.5$ mm, scattering is no longer observed after 15 min as the droplet has shrunk by 0.4 mm, which agrees well with optical microscopy observations (see supplementary table S2 and figure S3). At $z = 0.3$ mm in the 2D pattern, only $P(q)$ features in the form of distinct rings are present at short times (< 20 min), indicating that the dispersion is still quite dilute. After 20 min, these 2D patterns undergo a transformation, and a distinct inner ring with several peaks appears. This ring with peaks represents $S(q)$ features, indicating the formation of denser particle structures in the droplet. At $z = 0.1$ mm, $P(q)$ and $S(q)$ features are already present after

Figure 3. Selected 2D SAXS patterns of dried droplet assemblies (25 min) without an external magnetic field for (A) $m = 2.9$, (B) $m = 3.2$, (C) $m = 3.5$, (D) $m = 3.7$. (E) Model lines are plotted of the allowed ratio of the (hkl) diffraction peak position over the angle, α, for the predicted C_1 lattice. Experimental values ($m = 2.8$, 2.9, 3.2 3.5, and 3.7) of the peak position ratios are overlaid on top (markers).

15 min. Additionally, the average $I(q)$ intensity at $z = 0.1$ mm is higher because the beam completely hits the droplet, leading to a larger probed particle concentration [46], compared to near the top of the droplet where it interacts with both the droplet and the air above, potentially causing flares due to scattering at the droplet edge.

To further analyze the $S(q)$ peaks, we extracted the 1D $S(q)$ curves by taking the radial average of the 2D images, $I(q)$, and dividing by $P(q)$, which was experimentally collected from dilute capillaries and confirmed to match the initial SAXS patterns of the droplet experiments. Figure 2(E) displays selected $S(q)$ curves over time for $z = 0.3$ mm, where the evolution into several well-defined peaks, indicated by the vertical orange lines above the x-axis, is clearly visible. We fit the peak positions and widths with a pseudo-Voigt function [47] and obtained peak positions for the first four main peaks. After a drying time of 25 min, the peak positions were located at 7.87, 9.08, 12.73, and 15.14 μm^{-1}, where the peak located at 9.08 μm^{-1} appears less pronounced, resembling a shoulder adjacent to the first peak. These final positions are the same at the lower part of the droplet, specifically at $z = 0.1$ mm, as shown in figure 2(F). These positions are similar (within ± 0.01) to those expected for an fcc-like lattice, where the ratios of the first four peak positions to the first peak are 1, 1.15, 1.63, and 1.91. From our analysis we conclude that the superballs assemble into different fcc grains that are randomly oriented throughout the bulk of the droplet as well as on the surface. This result is consistent with the findings of Agthe *et al* [19], who demonstrated that the assembly of magnetic nano-cubes in a droplet resulted in a polycrystalline structure, with alignment near the droplet surface and randomly oriented clusters throughout the bulk. Our *in-situ* SAXS investigations of the drying droplets of superballs shows that we can obtain a detailed understanding of the evolution of droplet size and the formation of the superball structures.

3.3. Effect of superball shape

To examine how the shape of superball particles influences the structure formation, we analyzed dispersions consisting of superball particles with varying shapes, specifically with m values of 2.8, 2.9, 3.2, 3.5, and 3.7. Figure 3(A)–(D) depict the obtained 2D SAXS patterns from dried dispersion droplets ($\geqslant 25$ min) with four of these superballs. Here, we still observed scattering from the different assemblies at 0.5 mm, compared to our $m = 2.8$ assembly, even though the initial vol% is the same. This observation can be attributed to slight differences in the pinning position or the substrate position in the x-ray beam. For $m = 2.9$, the 2D patterns show broad $S(q)$ rings throughout the droplet, except near the top where two nearly vertical peaks are present at $q = 8.82$ μm^{-1}. However, these peaks are partially obscured due to the presence of strong flares related to the scattering from the edges of the droplet. For $m = 3.2$, we observe similar $S(q)$ rings and a difference in the 2D SAXS patterns near the top of the assembly (0.5 mm), where hexagonal symmetry in the $S(q)$ peaks is observed. Further increase in the shape parameter to $m = 3.5$ only reveals strong isotropic $S(q)$ rings throughout the height of the droplet. For our most cubic particles with $m = 3.7$, we observed a difference in the $S(q)$ pattern. In the early stages (see supplementary figure S5), the pattern exhibited isotropic behavior. However, as time progressed, it gradually shifted towards a faint hexagonal-like symmetry (figure 3(D)). This type of symmetry has also been observed in superball assemblies with higher cubicity ($m > 3.5$) when they form a brick-wall-like stacking in capillaries [13], suggesting that our particles are likely adopting a similar structure.
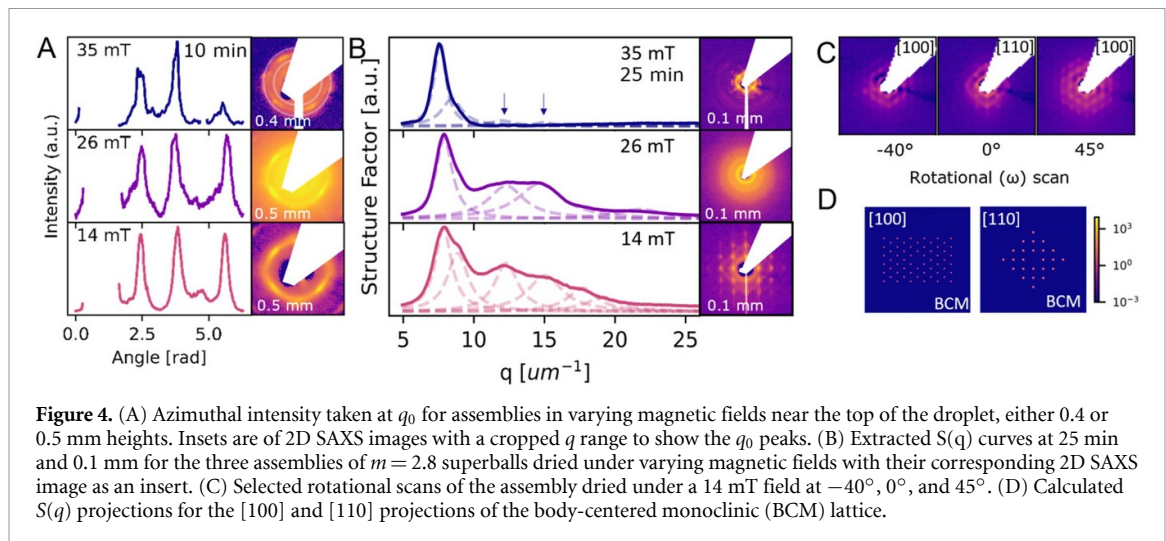
Previously, we found that the assembly of non-magnetic superballs in evaporating droplets form their predicted close-packed, albeit paracrystalline, rhombohedral lattices [29]. This result matched closely to a study by Meijer *et al* [8] where 3D capillary sediments of non-magnetic superballs would also nucleate into their predicted close-packed rhombohedral crystals. In this regard, we expect similarities in the close-packed structures that arise between these two types of assembly methods for the magnetic superballs. For capillary sediments of magnetic superballs, Meijer *et al* [13] demonstrated the formation of hexagonally stacked layers of superballs, with the specific stacking pattern depending on the shape of the superballs. Within these layers, it was hypothesized that the superballs adopted their predicted densest rhombohedral structures. Since the dried droplet assemblies of the magnetic superballs are polycrystalline, we compare the peak positions near the bottom of the droplet (0.1 mm) to the predicted close-packed rhombohedral superball structures. The C_1-lattice is a structure that describes a continuous transition from an fcc structure for $m = 2$ to a SC structure as $m \to \infty$. The structure can be characterized by the angle α, which transforms from 60° to 90° for fcc and SC, respectively (see references [7, 8, 29]). It has been shown that when superballs assemble into their densest packing, we can directly predict their expected angle, α, from the experimental m value [8, 29]. We note that as m increases from 2.8 to 3.7, we expect the angle, α, to increase from 66° to 71°. By utilizing the ratio of the diffraction peak position, we compared the experimentally measured ratio to the calculated ratio for C_1. The calculated ratio for C_1 is defined as $\frac{q_{hkl}}{q_{100}} = \left[\frac{(h^2 + k^2 + l^2)\sin\alpha^2}{\sin\alpha^2} + \frac{2(hk + kl + lh)(\cos\alpha^2 - \cos\alpha)}{\sin\alpha^2} \right]^{\frac{1}{2}}$ where q_{hkl} are the peak positions of allowed (*hkl*) reflections, as discussed in the supplementary information. Figure 3(E) provides a comprehensive analysis of the relationship between the observed experimental $S(q)$ peaks (markers) and the predicted C_1 lattice (lines) by examining the $\frac{q_{hkl}}{q_{100}}$ ratio. The second and, if present, third observed peaks in all samples exhibit a close alignment with the predicted lattice, indicating a strong correlation between particle shape and the formation of a rhombohedral lattice. This alignment suggests that the shape of the particles plays a significant role in determining the structure within the assemblies for droplet-based assemblies, which prevails over the magnetic dipole-dipole interactions. A similar behavior was observed for superball clusters (4–9 particles) formed in evaporating emulsion droplets, where both magnetic and nonmagnetic superball clusters with the same geometries exhibited comparable patterns [48, 49]. This observation demonstrates that the assembled structure resulting from spherical confinement over multiple length scales is primarily influenced by particle shape rather than interparticle interactions for this magnetic field strength. Additionally, this highlights the strong relationship between the *m*-value of the sample and the structures formed by magnetic superballs in evaporating droplets, further emphasizing the importance of particle shape in controlling the droplet-based self-assembly process.

3.4. Effect of magnetic field on evaporating droplets

Due to the presence of a magnetic moment inside the hematite core, we can control the orientation of the superballs and induce the formation of dipolar structures inside the droplets by applying a magnetic field [32] during drying. To investigate the effect of a magnetic field on our assemblies, we applied a uniform field of 14, 26, or 35 mT to drying 15 vol% dispersion droplets of $m = 2.8$ superballs. We observed distinctly different 2D SAXS patterns for the three droplets drying under varying magnetic field strengths. The most notable observation is the appearance of $S(q)$ peaks at the beginning of droplet evaporation. These $S(q)$ peaks exhibit different symmetries corresponding to the different field strengths, ranging from square for $\vec{B} = 14$ mT, to isotropic for $\vec{B} = 26$ mT, and finally to hexagonal for $\vec{B} = 35$ mT (see supplementary figure S4). The presence of diverse peak symmetries at an early stage suggests the formation of different ordered structures.

To compare the assembled structures at an early stage (at 10 min) under different magnetic fields, we examined the anisotropy within the inner-most $S(q)$ ring at q_0 by analyzing the azimuthal intensity for the corresponding q_0-value. Figure 4(A) presents a comparison of the azimuthal intensity profiles of different assemblies at q_0, located at $q = 7.58$, 7.85, and 7.69 μm^{-1} for magnetic field strengths of $\vec{B} = 14$, 26, and 35 mT, respectively. For the intermediate field strength (26 mT), we observed a notable decrease in the center-to-center pair separation distance ($d_{26\,\mathrm{mT}} = 0.80$ μm). Particles in the assembly may favor face-to-face orientations, resulting in a relatively compact configuration. Conversely, at both lower magnetic fields (14 mT) and higher magnetic fields (36 mT), the center-to-center pair separation distances increase, with $d_{14\,\mathrm{mT}} = 0.83$ μm and $d_{36\,\mathrm{mT}} = 0.82$ μm, respectively, which may result from a better dipolar alignment (corner-to-corner) [13, 32].

Importantly, for the top of the droplets at 10 min, we consistently observe a 4-fold anisotropy at q_0 across all assemblies, indicating similar local arrangements at the onset of structure formation. In most cases, this q_0 4-fold anisotropy persists throughout the height of the droplet with an exception in the 26 mT assembly, where isotropic rings are present except at the very top (0.5 mm, see supplementary figure S6). Furthermore, as we move lower into the 14 mT droplet at 10 min, the 4-fold anisotropy at q_0 persists, but additional higher

Figure 4. (A) Azimuthal intensity taken at q_0 for assemblies in varying magnetic fields near the top of the droplet, either 0.4 or 0.5 mm heights. Insets are of 2D SAXS images with a cropped q range to show the q_0 peaks. (B) Extracted S(q) curves at 25 min and 0.1 mm for the three assemblies of $m = 2.8$ superballs dried under varying magnetic fields with their corresponding 2D SAXS image as an insert. (C) Selected rotational scans of the assembly dried under a 14 mT field at $-40°$, $0°$, and $45°$. (D) Calculated $S(q)$ projections for the [100] and [110] projections of the body-centered monoclinic (BCM) lattice.

order Bragg peaks begin to emerge (supplementary figure S6). These additional peaks may suggest the presence of possible additional crystal phases or orientations throughout the droplet height.

In figure 4(B), we observe a transition from 6-fold symmetry (at 35 mT) to 4-fold symmetry (at 14 mT) within the insets of the 2D SAXS patterns. This 6-fold to 4-fold symmetry transition under magnetic fields aligns with previous observations in superball assemblies, especially when these lattices undergo rotation influenced by gravity [13]. To gain deeper insights into these structural changes, we extracted radial-averaged $S(q)$ curves from the 2D patterns at a specific time point, 25 min at $z = 0.1$ mm. Figure 4(B) presents these $S(q)$ curves (solid lines) for the three assemblies at various field strengths, along with corresponding 2D SAXS patterns. A clear change in $S(q)$ is observed across the spectrum, distinguishing 14 mT, 26 mT, and 35 mT. To characterize the anisotropic $S(q)$ patterns more accurately, we further extracted azimuthal wedges to pinpoint distinct $S(q)$ peak positions (see supplementary figure S7), which are also visually highlighted in figure 4(B), indicated by dashed lines. Examining the corresponding $S(q)$ plots, we note variations in the number of identified peaks among the assemblies: 6 peaks at 14 mT and 4 peaks at both 35 mT and 26 mT. Despite structural limitations at 26 mT due to broad peak sizes, a one-to-one comparison of peak positions (see supplementary table S3 and S4) suggests that the overall assembly structure remains relatively consistent between high and low magnetic fields. Additionally, we observe an increase in crystallinity, exemplified by the presence of higher-order Bragg peaks at lower magnetic field strengths. This suggests that more particle reorganizations can occur. Similarly, for superparamagnetic truncated nanocubes assembled via solvent evaporation, weak magnetic fields induce the formation of well-ordered 3D mesocrystals [50, 51]. This finding suggests that the applied magnetic field strength can be tuned to control and manipulate the degree of ordering in our assemblies.

The presence of high-ordered Bragg peaks in the assembly formed under a 14 mT field, allows us to further investigate the resultant structure by rotating the sample from $-60°$ to $+60°$. Figure 4(C) shows selected 2D SAXS patterns of $-40°$, $0°$, and $+45°$. Here, Bragg spots exhibiting square symmetry are visible, suggesting the presence of a crystal lattice with cubic characteristics. Previously, for 3D capillary sediments, magnetic superballs under a magnetic field assembled into a BCM lattice [13, 32]. Figure 4D shows the calculated contribution of the BCM lattice for the [100] and [110] projections, which is consistent with the experimental patterns in panel C. We observe clearly the [100] projections of the BCM lattice at $\omega = +45°$ and $-40°$ dictating a rotation of 85°. We determine the additional lattice parameters for the BCM lattice by tracking the position of the horizontal and vertical peak positions. The horizontal peaks in the [100] projections at $\omega = +40°$ and $-40°$ are $q = 12.79$ μm^{-1} and $q = 12.63$ μm^{-1}, respectively. The vertical peaks present in all rotations is located at $q = 7.89$ μm^{-1}. Then, the resulting lattice parameters for the BCM lattice are $a = 0.99$ μm, $b = 0.98$ μm, and $c = 1.52$ μm where $\alpha = \beta = 90°$ and $\gamma = 80°$. In the presence of very low magnetic fields the assembly of particles into a BCM lattice occurs while higher field strengths hinder its development. It is clear that there is a delicate balance between the strength of the magnetic attraction and the rate of aggregation. If the attraction is too strong, particles agglomerate quickly without re-orientation, resulting in dense deposits. Surprisingly, the confinement of the droplet has no effect on the creation of the BCM lattice, further emphasizing the complex interplay between magnetic field strength and particle interactions throughout the self-assembly process.
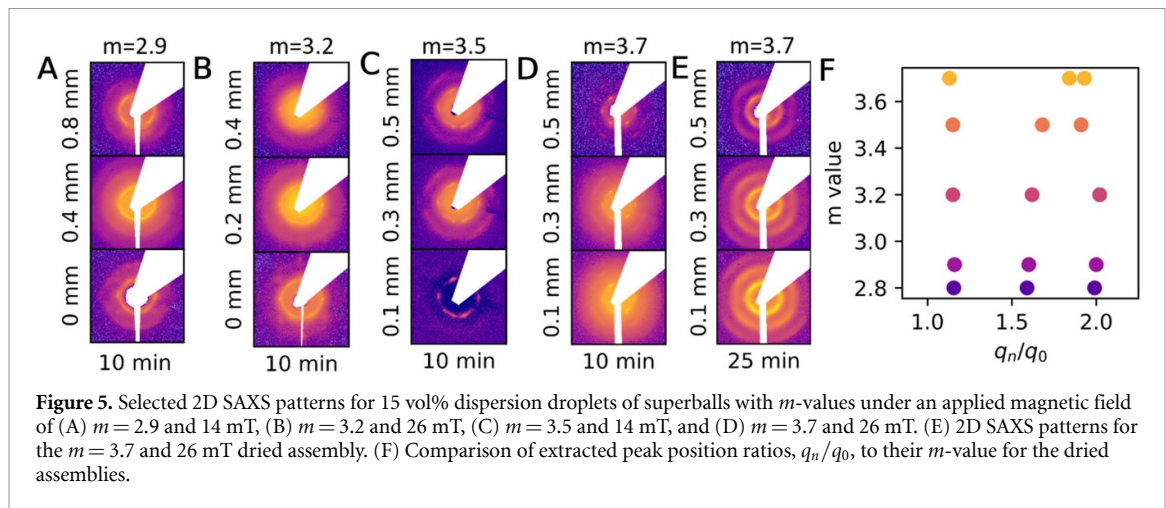
Figure 5. Selected 2D SAXS patterns for 15 vol% dispersion droplets of superballs with m-values under an applied magnetic field of (A) $m = 2.9$ and 14 mT, (B) $m = 3.2$ and 26 mT, (C) $m = 3.5$ and 14 mT, and (D) $m = 3.7$ and 26 mT. (E) 2D SAXS patterns for the $m = 3.7$ and 26 mT dried assembly. (F) Comparison of extracted peak position ratios, q_n/q_0, to their m-value for the dried assemblies.

3.5. Effect of superball shape and an applied field

To investigate the relationship between particle shape and structure formation under an applied magnetic field, we repeated the experiment in the magnetic field for particles with different m-values. For these samples, we utilized either a 14 mT or 26 mT magnetic field to prevent possible jamming effects observed at higher magnetic fields for $m = 2.8$ assemblies. Figures 5(A) and (B) show the 2D SAXS data at the initial stages of structure formation (10 min) for superballs of $m = 2.9$ and $m = 3.2$ within a 14 mT and 26 mT field, respectively, throughout the droplet's height. In both cases, we observed a structural behavior akin to that of the $m = 2.8$ superball assembly, characterized by the presence of a 4-fold anisotropy within the inner $S(q)$ ring located at $q_0 = 8.39\,\mu m^{-1}$ and $q_0 = 9.71\,\mu m^{-1}$ for assemblies of $m = 2.9$ and $m = 3.2$, respectively. These q_0 positions correspond to spacings of $d = 0.75\,\mu m$ and $d = 0.65\,\mu m$. These spacings are consistent with the characteristic length of the superballs, specifically $2a = 0.79\,\mu m$ and $0.68\,\mu m$ for $m = 2.9$ and 3.2, respectively. Therefore, the discrepancy in peak positions is attributed to variations in superball size at different m values.

At a droplet height of 0 mm, for the $m = 2.9$ assembly, faint Bragg peaks become discernible above the background intensity, located at $q_{1-3} = 9.87, 13.60$, and $17\,\mu m^{-1}$. Transitioning to superballs with greater cubicity ($m = 3.5$), we observed a different structural behavior as shown in figure 5(C). During the initial stages of structure formation (between 10 and 15 min), radially and azimuthally broad Bragg peaks appeared throughout the droplet's height. The azimuthal broadness of these reflections suggests a slight orientational mismatch among superball particles [52]. Upon reaching the most cubic superballs ($m = 3.7$), figure 5(D) shows the presence of clear hexagonally symmetric Bragg peaks throughout the droplet's height at the onset of structure formation (10 min). This robust hexagonal symmetry results from the brick-wall-like stacking of the superballs [13].

Despite the initial observation of similar hexagonal symmetries among assemblies, altering the cubicity of the superballs leads to different final structures (supplementary figures S8–11). Figure 5(E) shows the most striking change in final structure for the most cubic superballs where we observed a peak broadening in the azimuthal direction and a decrease in overall intensity until 20 min where the symmetry of the Bragg peaks switches from hexagonal to rectangular throughout the height of the droplet.

To compare the different structures, we calculated the ratio of the peak positions, q_n, and the first peak position, q_0, as shown in figure 5(F). For $m = 2.9$ and 3.2, the ratios correspond well to the BCM structure formed by the $m = 2.8$ assembly. This BCM structure has values of $q_n/q_0 = 1.15, 1.6$, and 2 highlighted earlier for $m = 2.8$ where 2.9 and 3.2 are within ± 0.02. However, as we increase the cubicity to $m = 3.5$, we see the ratio of the peak positions shift away from the BCM lattice where at $m = 3.7$ only the q_1/q_0 ratio remains similar at 1.13 compared to 1.14 for the $m = 2.8$ superball assembly. The overall peak positions after drying, paired with the significant difference in the peak ratios for $m = 3.7$ to all assemblies, indicates the presence of a different well-ordered structure arising from a transition to the brick-wall stacking. One potential explanation for this significant contrast may stem from the decreasing silica shell employed to coat the hematite superballs, particularly for higher m-values. As the shell thickness decreases, the particles experience intensified magnetic forces upon close proximity, since thicker silica shells increase the minimum distance between the magnetic cores [13, 32]. Additionally, the variation in the hematite core leads to different dipole moments [31]. Here, superballs with m-values of $2.8, 2.9$, and 3.2 share the same hematite

core, while superballs with *m*-values of 3.5 and 3.7 have a different core. Therefore, the change in dipole interactions has a strong effect on the resultant structure. Clearly, the interplay between the silica shell thickness, particle shape, and magnetic field strength are important parameters that determine the resultant superball assembly structure.

4. Conclusion

The self-assembly of magnetic superball particles confined in an evaporating droplet was investigated for a variety of changing parameters including the superball shape, *m*, and the external magnetic field strength. For micron-sized, silica-coated hematite superballs, we obtain free-standing macrostructures as we tune these two factors. Without an applied magnetic field, we observed the formation of polycrystalline structures with their expected densest rhombohedral symmetry for all *m*-values. While applying a high magnetic field hindered the assembly of magnetic superballs, we observed that at a lower magnetic field strength of 14 or 26 mT, well-defined symmetries emerged at the onset of structure formation. However, the ability of these well-defined structures to persist after the dewetting process varied significantly depending on the specific characteristics of the superballs. In particular, our observations revealed that well-ordered structures endured after dewetting for superballs with *m* = 2.8 and 3.7. These particular superballs, characterized by their roundest and most cubic shapes, exhibited a greater propensity to maintain the ordered structures. This observation highlights the significance of the colloid particle's shape, the presence of magnetic interactions, and the assembly within a confining droplet as crucial factors that collectively influence the formation and stability of well-ordered structures. Finally, the tunability of these parameters allows for the precise formation of macroscopic colloidal assemblies and holds promising potential for the creation of functional materials with customized properties on a macro-scale, paving the way for future advancements in material design and applications.

Data availability statement

The data that support the findings of this study are openly available at the following URL/DOI: http://doi. org/10.4121/4b4b1f8a-b32e-4d6f-974f-991c289925b6 [53].

ORCID iDs

S Schyck ⦿ https://orcid.org/0000-0002-9731-2160
J-M Meijer ⦿ https://orcid.org/0000-0002-5148-9948
M P M Schelling ⦿ https://orcid.org/0000-0002-6704-9007
A V Petukhov ⦿ https://orcid.org/0000-0001-9840-6014
L Rossi ⦿ https://orcid.org/0000-0002-0215-5386

References

[1] Bozorg Bigdeli M B and Amy Tsai P A 2020 Making photonic crystals via evaporation of nanoparticle-laden droplets on superhydrophobic microstructures *Langmuir* **36** 4835–41
[2] Quan Z and Fang J 2010 Superlattices with non-spherical building blocks *Nano Today* **5** 390–411
[3] Waterhouse G I N and Waterland M R 2007 Opal and inverse opal photonic crystals: fabrication and characterization *Polyhedron* **26** 356–68
[4] Vogel N, Utech S, England G T, Shirman T, Phillips K R, Koay N, Burgess I B, Kolle M, Weitz D A and Aizenberg J 2015 Color from hierarchy: diverse optical properties of micron-sized spherical colloidal assemblies *Proc. Natl Acad. Sci.* **112** 10845–50
[5] Glotzer S C and Solomon M J 2007 Anisotropy of building blocks and their assembly into complex structures *Nat. Mater.* **6** 557–62
[6] Hong Lee Y H, Leng Lay C L, Shi W, Kwee Lee H K, Yang Y, Li S and Yi Ling X Y 2018 Creating two self-assembly micro-environments to achieve supercrystals with dual structures using polyhedral nanoparticles *Nat. Commun.* **9** 2769
[7] Jiao Y, Stillinger F H and Torquato S 2009 Optimal packings of superballs *Phys. Rev.* E **79** 041309
[8] Meijer J-M, Pal A, Ouhajji S, Lekkerkerker H N W, Philipse A P and Petukhov A V 2017 Observation of solid-solid transitions in 3D crystals of colloidal superballs *Nat. Commun.* **8** 14352

[9] Batten R D, Stillinger F H and Torquato S 2010 Phase behavior of colloidal superballs: shape interpolation from spheres to cubes *Phys. Rev.* E **81** 061105

[10] Ni R, Prasad Gantapara A P, de Graaf J, van Roij R and Dijkstra M 2012 Phase diagram of colloidal hard superballs: from cubes via spheres to octahedra *Soft Matter* **8** 8826–34

[11] Zhang Y, Lu F, van der Lelie D and Gang O 2011 Daniel van der Lelie and Oleg Gang. Continuous phase transformation in nanocube assemblies *Phys. Rev. Lett.* **107** 135701

[12] Brunner J, Baburin I A, Sturm S, Kvashnina K, Rossberg A, Pietsch T, Andreev S, Sturm (née Rosseeva) E and Cölfen H 2017 Self-assembled magnetite mesocrystalline films: toward structural evolution from 2D to 3D superlattices *Adv. Mater. Interfaces* **4** 1600431

[13] Meijer J-M, Byelov D V, Rossi L, Snigirev A, Snigireva I, Philipse A P and Petukhov A V 2013 Self-assembly of colloidal hematite cubes: a microradian x-ray diffraction exploration of sedimentary crystals *Soft Matter* **9** 10729–38

[14] Ahniyaz A, Sakamoto Y and Bergström L 2007 Magnetic field-induced assembly of oriented superlattices from maghemite nanocubes *Proc. Natl Acad. Sci.* **104** 17570–4

[15] Li Z, Fan Q and Yin Y 2022 Colloidal self-assembly approaches to smart nanostructured materials *Chem. Rev.* **122** 4976–5067

[16] Yadav A and Tirumkudulu M S 2017 Free-standing monolayer films of ordered colloidal particles *Soft Matter* **13** 4520–5

[17] Yu Y, Yang Xi, Liu M, Nishikawa M, Tei T and Miyako E 2019 Amphipathic nanodiamond supraparticles for anticancer drug loading and delivery *ACS Appl. Mater. Interfaces* **11** 18978–87

[18] Liu J, Xiao M, Li C, Li H, Wu Z, Zhu Q, Tang R, Xu A B and He L 2019 Rugby-ball-like photonic crystal supraparticles with non-close-packed structures and multiple magneto-optical responses *J. Mater. Chem.* **7** 15042–8

[19] Agthe M, Plivelic T S, Labrador A, Bergström L and Salazar-Alvarez G 2016 Following in real time the two-step assembly of nanoparticles into mesocrystals in levitating drops *Nano Lett.* **16** 6838–43

[20] Kapuscinski M, Agthe M, Lv Z-P, Liu Y, Segad M and Bergström L 2020 Temporal evolution of superlattice contraction and defect-induced strain anisotropy in mesocrystals during nanocube self-assembly *ACS Nano* **14** 5337–47

[21] de Nijs B, Dussi S, Smallenburg F, Meeldijk J D, Groenendijk D J, Filion L, Imhof A, van Blaaderen A and Dijkstra M 2015 Entropy-driven formation of large icosahedral colloidal clusters by spherical confinement *Nat. Mater.* **14** 56–60

[22] Rastogi V, Melle S, Calderón O G, García A A, Marquez M and Velev O D 2008 Synthesis of light-diffracting assemblies from microspheres and nanoparticles in droplets on a superhydrophobic surface *Adv. Mater.* **20** 4263–8

[23] Kim J, Hwang H, Butt H-J and Wooh S 2021 Designing the shape of supraparticles by controlling the apparent contact angle and contact line friction of droplets *J. Colloid Interface Sci.* **588** 157–63

[24] Tirumkudulu M S 2018 Buckling of a drying colloidal drop *Soft Matter* **14** 7455–61

[25] Seyfert C, Berenschot E J W, Tas N R, Susarrey-Arce A and Marin A 2021 Evaporation-driven colloidal cluster assembly using droplets on superhydrophobic fractal-like structures *Soft Matter* **17** 506–15

[26] Wang D *et al* 2021 Binary icosahedral clusters of hard spheres in spherical confinement *Nat. Phys.* **17** 128–34

[27] Wang J, Fru Mbah C F, Przybilla T, Apeleo Zubiri B, Spiecker E, Engel M and Vogel N 2018 Magic number colloidal clusters as minimum free energy structures *Nat. Commun.* **9** 5259

[28] Lv Z-P, Kapuscinski M and Bergström L 2019 Tunable assembly of truncated nanocubes by evaporation-driven poor-solvent enrichment *Nat. Commun.* **10** 4228

[29] Schyck S, Meijer J-M, Baldauf L, Schall P, Petukhov A V and Rossi L 2022 Self-assembly of colloidal superballs under spherical confinement of a drying droplet *JCIS Open* **5** 100037

[30] Sugimoto T and Sakata K 1992 Preparation of monodisperse pseudocubic α-Fe$_2$O$_3$ particles from condensed ferric hydroxide gel *J. Colloid Interface Sci.* **152** 587–90

[31] Meijer J M and Rossi L 2021 Preparation, properties and applications of magnetic hematite microparticles *Soft Matter* **17** 2354–68

[32] Rossi L, Donaldson J G, Meijer J-M, Petukhov A V, Kleckner D, Kantorovich S S, Irvine W T M, Philipse A P and Sacanna S 2018 Self-organization in dipolar cube fluids constrained by competing anisotropies *Soft Matter* **14** 1080–7

[33] Graf C, Vossen D L J, Imhof A and van Blaaderen A 2003 A general method to coat colloidal particles with silica *Langmuir* **19** 6693–700

[34] Rossi L, Sacanna S, Irvine W T M, Chaikin P M, Pine D J and Philipse A P 2011 Cubic crystals from cubic colloids *Soft Matter* **7** 4139–42

[35] Rossi L, Soni V, Ashton D J, Pine D J, Philipse A P, Chaikin P M, Dijkstra M, Sacanna S and Irvine W T M 2015 Shape-sensitive crystallization in colloidal superball fluids *Proc. Natl Acad. Sci.* **112** 5286–90

[36] Petukhov A V, Meijer J-M and Jan Vroege G J 2015 Particle shape effects in colloidal crystals and colloidal liquid crystals: small-angle x-ray scattering studies with microradian resolution *Curr. Opin. Colloid Interface Sci.* **20** 272–81

[37] Snigirev A, Kohn V, Snigireva I and Lengeler B 1996 A compound refractive lens for focusing high-energy x-rays *Nature* **384** 49–51

[38] Bras W, Dolbnya I, Detollenaere D, Van Tol R, Malfois M, Greaves G, Ryan A and Heeley E 2003 Recent experiments on a small-angle/wide-angle x-ray scattering beam line at the ESRF *J. Appl. Crystallogr.* **36** 791–4

[39] Elkies N D, Odlyzko A M and Rush J A 1991 On the packing densities of superballs and other bodies *Invent. Math.* **105** 613–39

[40] Skov Pedersen J S 1997 Analysis of small-angle scattering data from colloids and polymer solutions: modeling and least-squares fitting *Adv. Colloid Interface Sci.* **70** 171–210

[41] Biehl R 2019 Jscatter, a program for evaluation and analysis of experimental data *Plos One* **14**

[42] ten Napel D N, Meijer J-M and Petukhov A V 2021 The analysis of periodic order in monolayers of colloidal superballs *Appl. Sci.* **11** 5117

[43] Rastogi V, García A A, Marquez M and Velev O D 2010 Anisotropic particle synthesis inside droplet templates on superhydrophobic surfaces *Macromol. Rapid Commun.* **31** 190–5

[44] Pan Z, Dash S, Weibel J A and Garimella S V 2013 Assessment of water droplet evaporation mechanisms on hydrophobic and superhydrophobic substrates *Langmuir* **29** 15831–41

[45] Barmi M R and Meinhart C D 2014 Convective flows in evaporating sessile droplets *J. Phys. Chem.* B **118** 2414–21

[46] Sen D, Bahadur J, Mazumder S, Santoro G, Yu S and Roth S V 2014 Probing evaporation induced assembly across a drying colloidal droplet using in situ small-angle x-ray scattering at the synchrotron source *Soft Matter* **10** 1621–7

[47] Olivero J J and Longbothum R L 1977 Empirical fits to the voigt line width: a brief review *J. Quant. Spectrosc. Radiat. Transfer* **17** 233–6

[48] Donaldson J G, Schall P and Rossi L 2021 Magnetic coupling in colloidal clusters for hierarchical self-assembly *ACS Nano* **15** 4989–99

[49] Baldauf L, Teich E G, Schall P, van Anders G and Rossi L 2022 Shape and interaction decoupling for colloidal preassembly *Sci. Adv.* **8** eabm0548

[50] Disch S, Wetterskog E, Hermann R P, Salazar-Alvarez G, Busch P, Brückel T, Bergström L and Kamali S 2011 Shape induced symmetry in self-assembled mesocrystals of iron oxide nanocubes *Nano Lett.* **11** 1651–6

[51] Disch S *et al* 2013 Structural diversity in iron oxide nanoparticle assemblies as directed by particle morphology and orientation *Nanoscale* **5** 3969–75

[52] Förster S, Timmann A, Schellbach C, Frömsdorf A, Kornowski A, Weller H, Roth S V and Lindner P 2007 Order causes secondary bragg peaks in soft materials *Nat. Mater.* **6** 888–93

[53] Schyck S ,Meijer J-M, Schelling M P M, Petukhov A V, and Rossi L Data for droplet-based assembly of magnetic superballs, Version 1. dataset (*4TU.ResearchData.*) (https://doi.org/10.4121/4b4b1f8a-b32e-4d6f-974f-991c289925b6)